CHALMERS
UNIVERSITY OF TECHNOLOGY

Software-Defined Radio Testbed for 6G Research

Experimental Integration of SDR-based User Equipment into a D-MIMO Testbed

Bachelor's Thesis in Electrical Engineering

Sajeel Ahmad, Niclas Collard, Martin Martinsson, Gabriel Mörck, Sammy Rahimi

DEPARTMENT OF ELECTRICAL ENGINEERING
CHALMERS UNIVERSITY OF TECHNOLOGY
Gothenburg, Sweden 2026
www.chalmers.se

Bachelor´s Thesis 2026

Software-Defined Radio Testbed for 6G Research

Experimental Integration of SDR-based User Equipment into a D-MIMO Testbed

Sajeel Ahmad, Niclas Collard, Martin Martinsson, Gabriel Mörck, Sammy Rahimi

CHALMERS
UNIVERSITY OF TECHNOLOGY

Department of Electrical Engineering
Division of Communications, Antennas, and Optical Networks
Chalmers University of Technology
Gothenburg, Sweden 2026

Software-Defined Radio Testbed for 6G Research

Supervisor: Kaan Okumus, Division of Communications, Antennas, and Optical Networks
Examiner: Erik Ström, Division of Communications, Antennas, and Optical Networks

Bachelor Thesis 2026
Department of Electrical Engineering
Division of Communication, Antennas, and Optical Networks
Chalmers University of Technology
SE-412 96 Gothenburg
Sweden
Telephone +46 31 772 1000

Cover: Image of a USRP B205mini-i with an antenna connected to the TX port.

Typeset in LaTeX
Gothenburg, Sweden 2026

Abstract

The increasing demand for wireless communication and the limitations of current cellular networks motivate research into new cellular network architectures. Traditionally, the philosophy in cellular networks has been to have one base station per geographical area, and that a cellular user is only connected to one base station at a time. This has limitations with regard to uneven coverage and poor cellular quality far from base stations. Distributed multiple-input multiple-output (D-MIMO) systems aim to resolve those limitations, providing users with improved cellular network performance. Chalmers University of Technology has a D-MIMO testbed that is used in research. Although the testbed fulfills its intended purpose, its current setup is based on costly laboratory equipment, which limits experimental flexibility and restricts scalability. Therefore, this thesis aims to implement a more flexible and cost-effective method to emulate user equipment in the current testbed. The project first focused on designing and validating a point-to-point communication link between two software-defined radios, evaluating several key aspects of the radios, including bandwidth limitations, maximum achievable throughput, and limitations related to signal duration and onboard memory. The results show that the system can operate with a maximum bandwidth of 49.51 MHz and a maximum throughput of 54.25 Mbit/s. The developed communication system enables reliable data transmission and reception, using preambles to detect and correct transmission errors and verify the accuracy of the transmitted data. It operates without external reference signals and compensates for carrier frequency offsets. Bit error rate (BER) and error vector magnitude (EVM) were used to evaluate the system. In indoor conditions, a BER of 0 and an EVM of 6.25% were achieved, allowing it to transmit data reliably between two radios. The system was also successfully integrated into the D-MIMO testbed, where it was subjected to strict synchronization constraints. The transmitted signal was successfully received by all six remote radio heads and combined using maximum ratio combining, achieving a BER of 0 and an EVM of 4.64%.

Keywords: 6G testbed, USRP, software-defined radio, distributed MIMO.

Acknowledgements

We would like to express our gratitude to those who contributed to this project through their guidance, support, and technical expertise throughout the course of this thesis work.

First, we would like to thank our supervisor, Kaan Okumus, for his continuous feedback, valuable discussions, and support throughout this project. His guidance played an important role in both the technical development of the systems and the completion of this thesis.

We would also like to thank our technical advisor, Frida Olofsson, for her assistance and support during the integration and testing of the D-MIMO testbed. Her help during the testbed experiments was highly appreciated.

In addition, we would like to thank our examiner, Erik Ström, for his feedback, encouragement, and engagement during this project. His insights and discussions helped strengthen the overall quality of the work.

Sajeel Ahmad, Niclas Collard, Martin Martinsson, Gabriel Mörck, Sammy Rahimi,
Gothenburg, May 2026

Contents

List of Acronyms

Below is the list of acronyms that have been used throughout this thesis listed in alphabetical order:

6G	Sixth generation (wireless communication)
ADC	Analog-to-digital converter
AWGN	Additive white Gaussian noise
BER	Bit error rate
BPSK	Binary phase shift keying
CFO	Carrier frequency offset
DAC	Digital-to-analog converter
D-MIMO	Distributed multiple-input multiple-output
EVM	Error vector magnitude
FPGA	Field-programmable gate array
IQ	In-phase, quadrature
ISI	Intersymbol interference
LO	Local oscillator
MRC	Maximum ratio combining
OBW	Occupied bandwidth
PN	Pseudorandom noise
QPSK	Quadrature phase shift keying
RRH	Remote radio head
RRC	Root-raised-cosine
RX	Receiver
SDR	Software-defined radio
SNR	Signal-to-noise ratio
TX	Transmitter
USRP	Universal software radio peripheral

List of Figures

List of Tables

1

Introduction

1.1 Background

Cellular communication systems constitute one of the most critical infrastructures in modern society. Applications ranging from smartphones and connected vehicles to industrial automation and remote healthcare rely on the continuous exchange of information over mobile networks [1]. With each new generation of cellular technology, these capabilities have expanded, and the transition to sixth-generation (6G) systems is expected to enable even more transformative use cases [2].

To support these ambitions, future networks are expected to rely on advanced radio architectures. One such key technology is distributed multiple-input multiple-output (D-MIMO), where a large number of geographically separated antennas cooperate to serve users. Compared to conventional cellular systems, D-MIMO can improve coverage, spectral efficiency, and energy performance [3], [4]. At the same time, it introduces stringent requirements on synchronization between user equipment and base stations [4].

At Chalmers University of Technology, a D-MIMO testbed has been developed to study such systems. The testbed employs multiple base stations interconnected via analog radio-over-fiber links and operates in a time-division duplexing mode at a carrier frequency of 2.35 GHz. In the current setup, user equipment is emulated using laboratory instruments such as oscilloscopes and function generators. While this approach provides accurate signal generation, the required equipment is expensive and limits the scalability and flexibility of experimental evaluations. Consequently, there is a strong motivation to investigate more cost-effective and adaptable alternatives for user emulation.

Software-defined radios (SDRs) are a suitable solution in this context. In an SDR system, many radio functions that are traditionally implemented in hardware are instead handled in software, which makes the system highly flexible and reconfigurable. This makes it possible to change transmission and reception parameters in real time and simplifies rapid prototyping of communication systems. Previous studies have shown that SDR platforms are well-suited for experimental wireless communication setups [5]. In particular, universal software radio peripheral (USRP) provides a

flexible hardware platform that can be used to emulate realistic user equipment in a D-MIMO testbed environment [5]. However, a flexible and experimentally validated SDR-based user equipment solution for the Chalmers D-MIMO testbed is still missing.

1.2 Project goal and research questions

The goal of this project is to design, implement, and evaluate an SDR-based user equipment for use in the Chalmers D-MIMO research testbed. The proposed user equipment is the USRP B205mini-i and is intended to replace existing laboratory instruments currently used for user emulation, enabling a more cost-effective, scalable, and adaptable experimental setup.

The developed system should be capable of transmitting and receiving baseband in-phase and quadrature (IQ) samples and operating coherently with the existing D-MIMO testbed at Chalmers University of Technology. To achieve this, the project is structured into two main phases. In the first phase, a point-to-point communication link between two USRPs is designed and validated to verify basic transmission and reception functionality, including digital modulation, filtering, and performance evaluation. In the second phase, the USRP-based user equipment is integrated into the D-MIMO testbed, where its ability to operate under synchronization constraints and interact with multiple distributed access points connected to a central processing unit is investigated.

The project aims to address the following research questions

- What is the maximum achievable throughput measured in bits per second, under indoor laboratory conditions?
- What is the maximum usable signal bandwidth that can be achieved using the USRP B205mini-i platform in the considered experimental setup?
- What is the maximum signal duration that can be transmitted and received, given the available on-board memory and data transfer constraints of the USRPs?
- To what extent can the USRP-based user equipment be synchronized with the D-MIMO testbed when not using external reference clocks and timing signals?

1.3 Scopes and limitations

This project focuses on the design and experimental evaluation of USRP-based user equipment operating at the physical layer. The work is limited to baseband signal generation, digital modulation and demodulation, filtering, and synchronization with the existing D-MIMO testbed. The system is intended for controlled laboratory experiments and does not represent a complete end-to-end communication system.

The project is carried out using the USRP B205mini-i platform and is therefore constrained by its hardware specifications [6]:

- Carrier frequency range of 70 MHz to 6 GHz
- Maximum instantaneous bandwidth of up to 56 MHz
- Synchronization via a 10 MHz reference clock and a pulse-per-second signal

Higher-layer communication features such as medium access control and error correction codes are not considered. Communication is limited to half-duplex operation, and advanced features such as adaptive modulation, channel coding, and link adaptation are outside the scope of this work. Experimental evaluations are performed using a limited number of USRP devices in an indoor laboratory environment. Therefore, large-scale deployments and outdoor measurements are not considered. Furthermore, the wireless channel is modeled under a line-of-sight assumption, neglecting effects such as multipath fading.

2

System Model

Wireless communication systems are commonly modeled as three separate stages: the transmitter, the communication channel, and the receiver. In this chapter, a brief overview of the assumed system model is presented, with particular emphasis on channel and hardware impairments. A brief overview of the existing D-MIMO testbed at Chalmers is also presented.

2.1 Transmitter

In wireless communication systems, the transmitter is responsible for generating and preparing information for wireless propagation through the communication channel. The transmission process begins with the generation of digital data, which is represented as discrete-time symbols. These samples are then processed through several signal processing stages, including modulation, pulse shaping, and amplification, to create a waveform suitable for transmission.

Modulation

Modulation is a fundamental technique in communication systems in which information is embedded into an analog signal for transmission over a communication channel. In digital communication systems, the information is represented as binary bits that are mapped to variations in the transmitted waveform. To efficiently utilize the available radio spectrum, multiple bits are grouped together and represented by symbols rather than transmitting each bit individually. Digital baseband signals are commonly represented using IQ components, forming complex-valued baseband samples. The baseband representation is centered around 0 Hz, meaning that the signal spectrum is located symmetrically around the origin in the frequency domain before being shifted to a carrier frequency for transmission. A complex baseband symbol a_k can be expressed as [7]

$$a_k = I + jQ, \tag{2.1}$$

where I represents the in-phase component and Q represents the quadrature component. From this notation, the symbol a_k is represented as a complex IQ-sample. Together, these components define both the amplitude and phase of the transmitted symbol. By allowing several bits to be mapped onto a single symbol, different

combinations of amplitude and phase can therefore represent different bit patterns. A modulation technique that employs this functionality is quadrature phase shift keying (QPSK). In QPSK, the signal can assume four different phase values. These phases are separated by 90°, and each corresponds to a specific pair of bits: 00, 01, 10, or 11 as shown in Figure 2.1.

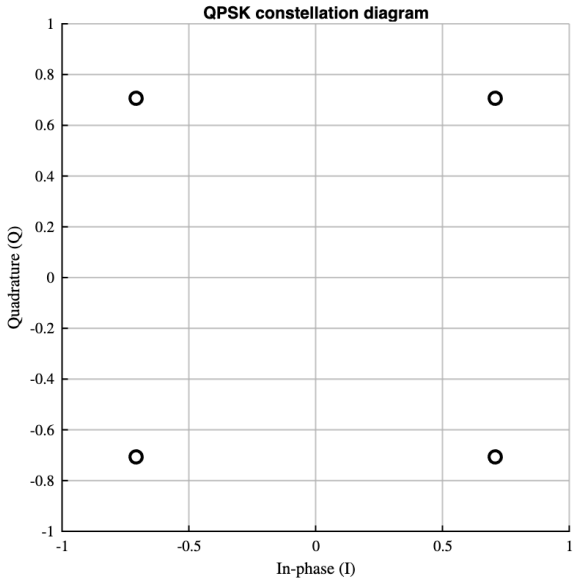

Figure 2.1: Constellation diagram of QPSK.

Pulse shaping

At the transmitter, each symbol is not sent as an ideal impulse but is instead shaped by a pulse of finite duration. Pulse shaping confines the signal to a well-defined bandwidth and reduces out-of-band emissions [7]. Before pulse shaping, the symbol sequence is typically upsampled by inserting additional samples between symbols. This increases the sampling rate, enabling the pulse-shaping filter to generate smoother transitions between symbols. The upsampling factor is commonly referred to as the number of samples per symbol, N_s. After pulse shaping and upsampling, the signal is usually turned into a continuous waveform by a digital-to-analog converter (DAC). The resulting analog signal is subsequently upconverted to passband by a mixer driven by an oscillator operating at the carrier frequency f_c. Figure 2.2 illustrates a simplified block diagram of the transmitter.

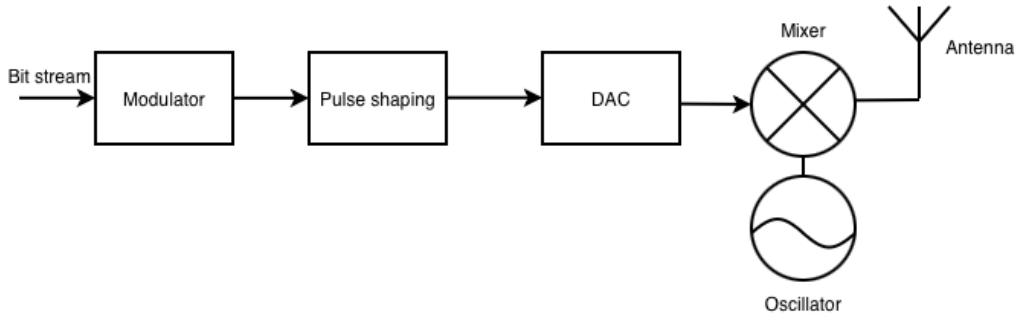

Figure 2.2: Simplified block diagram of the transmitter signal chain.

2.2 Channel and signal model

During transmission between a transmitter and a receiver, the signal is degraded by various distortions and impairments introduced by the wireless channel and radio hardware. In addition, synchronization errors may occur. These effects distort the transmitted information, making it essential for the receiver to compensate for these effects.

Noise

In wireless communication systems, noise is an unavoidable phenomenon that degrades the quality of the transmitted signal and limits overall system performance. Noise can originate from several sources, including interference from other wireless transmissions, atmospheric disturbances, and thermal noise generated by the random motion of electrons in electronic components such as amplifiers, antennas, and receivers [8].

A commonly used model for representing noise in communication systems is the additive white Gaussian noise (AWGN) model. The AWGN model is used due to its mathematical simplicity and its ability to accurately approximate thermal noise in many practical systems. The term additive indicates that the noise is added directly to the transmitted signal, white refers to the assumption that the noise has a constant power spectral density across all frequencies, and Gaussian implies that the noise amplitudes follow a normal distribution. The received signal in an AWGN channel can be expressed as

$$r[n] = x[n] + w[n]. \tag{2.2}$$

Here, $r[n]$ denotes the received signal, $x[n]$ is the transmitted signal, and $w[n]$ represents the AWGN noise in discrete-time. The noise process is commonly modeled as a zero-mean Gaussian random variable with variance $N_0/2$, given by $w[n] \sim \mathcal{N}(0, N_0/2)$ where N_0 represents the noise power spectral density [9]. An illustrated example showing the effect of AWGN on a QPSK signal constellation is presented in Figure 2.3.

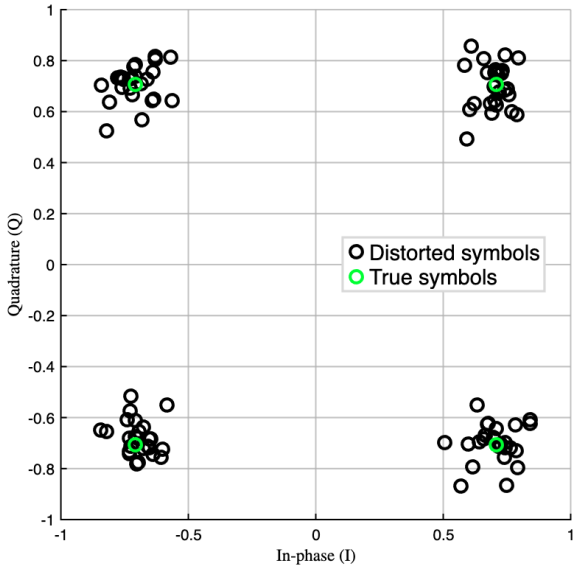

Figure 2.3: Illustration of a constellation with AWGN. SNR set to 25 dB on 100 symbols.

Carrier frequency offset

Local oscillators (LO) in radios have small hardware imperfections, causing the transmitter and receiver oscillators to operate at slightly different frequencies, even when configured identically. This mismatch creates a carrier frequency offset (CFO), which introduces a continuous phase rotation in the received signal [10]. A received signal subject to CFO can be mathematically expressed as

$$r[n] = x[n]e^{j2\pi\frac{\Delta f}{f_s}n}, \tag{2.3}$$

where $\Delta f/f_s$ denotes the fractional CFO between the transmitter and receiver LOs, and n is the discrete-time sampling index. A visualized example of how CFO affects the baseband symbols of a QPSK constellation is depicted in Figure 2.4.

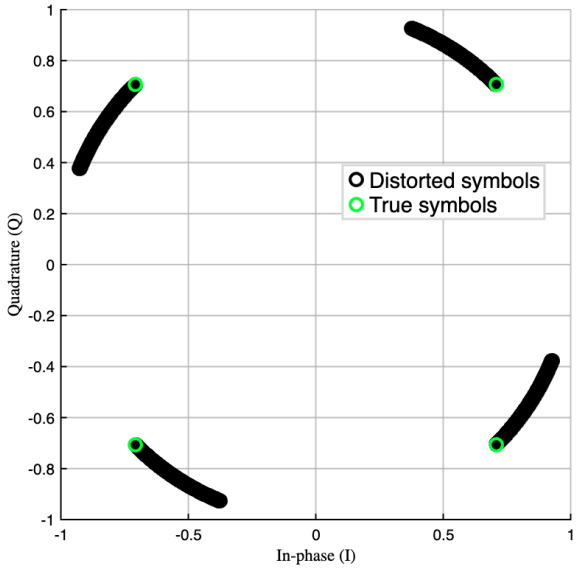

Figure 2.4: Illustration of a constellation subject to CFO. $\Delta f/f_s = 0.0001$ and 4000 symbols.

Phase offset

The receiver interprets the transmitted symbol relative to its own LO. This means that if the LO of the transmitter does not share the same phase as the receiver's LO, the received symbols will have a constant phase offset in the complex plane compared to the transmitted constellation [10]. Mathematically, a received signal subject to a constant phase offset can be expressed as

$$r[n] = x[n]e^{j\phi}. \tag{2.4}$$

Here, ϕ represents the constant phase offset. A visualized example of a QPSK constellation subject to a phase offset is illustrated in Figure 2.5.

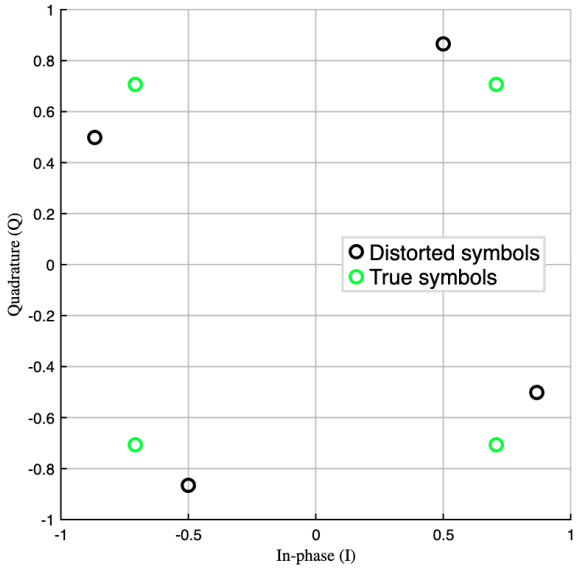

Figure 2.5: Illustration of constellation with a constant phase offset $\phi = \pi/12$.

Mathematical signal model

The complete received discrete-time baseband signal, accounting for the previously described channel and hardware impairments, can be modeled as

$$r[n] = x[n]e^{j\left(2\pi\frac{\Delta f}{f_s}n+\phi\right)} + w[n], \tag{2.5}$$

where

- $r[n]$ is the received discrete-time complex baseband signal,
- $x[n]$ is the transmitted discrete-time complex baseband signal,
- $\frac{\Delta f}{f_s}$ is the fractional carrier frequency offset between the transmitter and receiver oscillators,
- ϕ is the phase offset between the transmitter and receiver,
- $w[n]$ represents additive noise and interference,
- n is the discrete-time sample index.

2.3 Receiver

The receiver is responsible for extracting and reconstructing the original information from a corrupted version of the transmitted waveform. The reception process begins with the capture of a noisy, attenuated, and distorted signal as it arrives through the communication channel. This signal is then processed through several signal

processing stages, including downconversion, matched filtering, synchronization, and demodulation to recover the transmitted digital data as discrete-time IQ samples.

Matched filter

A matched filter is a linear filter designed to maximize the signal-to-noise ratio (SNR) at the receiver in the presence of AWGN. The filter is matched to the transmitted pulse-shaping filter by using a time-reversed and delayed version of the transmitted pulse shape. In practice, the received signal is passed through the filter using convolution, which effectively performs a correlation with the known pulse shape. This process concentrates the signal energy at the sampling instant [11]. Before matched filtering, the received continuous-time signal is typically downconverted to baseband using a mixer and an oscillator. The resulting baseband signal is then sampled by an analog-to-digital converter (ADC), producing a discrete-time signal suitable for digital signal processing. A simplified receiver block diagram is shown in Figure 2.6.

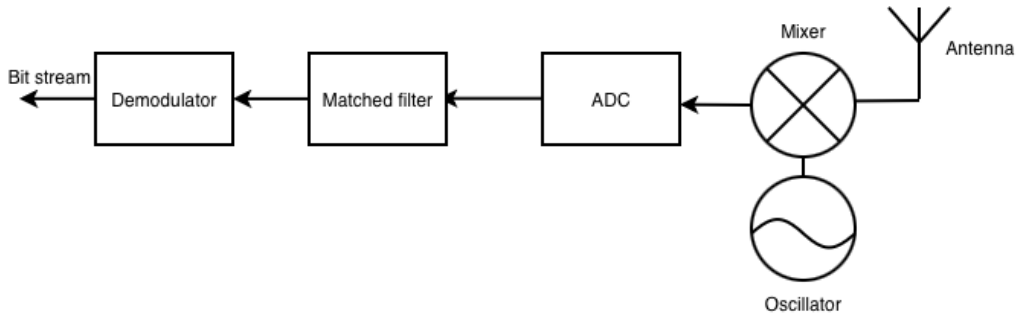

Figure 2.6: Simplified block diagram of the receiver chain.

2.4 Distributed MIMO testbed

As illustrated in Figure 2.7, the Chalmers D-MIMO testbed consists of 6 remote radio heads (RRH) that function as receiving units, which are interconnected via fiber links. Each RRH is connected to the same LO, ensuring that no CFO occurs. This is essential in D-MIMO systems, where coherent transmission from each RRH is required to achieve accurate beamforming at the user [12]. Conversely, when a user transmits a signal, it is independently received by all RRHs, and the signals collected at each RRH are subsequently superimposed at the field-programmable gate array (FPGA). The received signal at antenna i can be modeled as

$$r_i[n] = h_i x[n] + w[n], \tag{2.6}$$

where h_i represents the channel gain experienced by the transmitted signal before reaching antenna i.

The testbed supports signal bandwidths up to 80 MHz. However, the FPGA is constrained by limited on-chip memory, which restricts the maximum length of signals that can be processed. The maximum signal duration supported by the testbed is 76.8 μs.

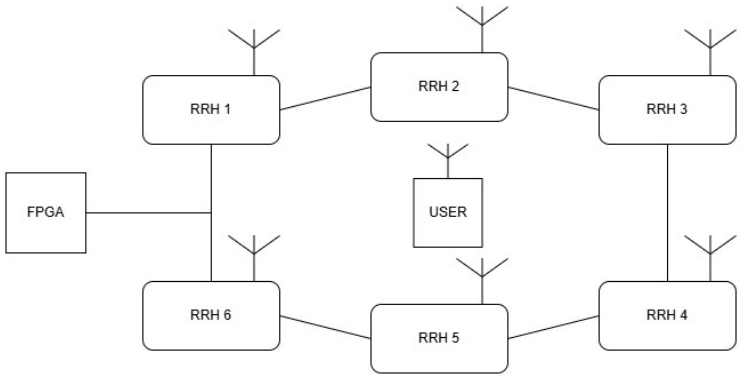

Figure 2.7: Illustration of the D-MIMO testbed at Chalmers. Six RRHs are interconnected via fiber and linked to a shared FPGA.

3

Theoretical Background

This chapter introduces the fundamental techniques and algorithms used in the experimental work. The topics covered include digital modulation techniques, signal processing methods for interference mitigation, synchronization mechanisms for reliable symbol detection, and techniques for compensating signal distortion. These concepts form the theoretical foundation for the system design and implementation described in subsequent chapters.

3.1 Symbol demodulation and gray code

Symbol demodulation

When the filtered signal is received and sampled, a decision on the symbol is needed. This is the task of symbol demodulation. For QPSK, the phase variations are represented by symbols, denoted as a_k. The total number of possible symbols in a modulation scheme is referred to as M, where all symbols belong to an alphabet $\mathcal{A}$. Using the maximum likelihood criterion, the receiver selects the symbol that most likely was transmitted, given the observed distorted sample. This corresponds to choosing the constellation point with the minimum Euclidean distance to the received value, expressed as

$$\hat{a} = \arg\min_{a_k \in \mathcal{A}} \|r - a_k\|^2, \tag{3.1}$$

where r is the received sample and $\hat{a}$ is the estimated symbol.

Gray code

Gray coding is used to minimize the impact of symbol errors on the bit error rate (BER). Since adjacent constellation points differ only by one bit, a symbol error caused by noise would shift a received symbol to a neighboring point [13]. This results in a single bit error rather than two bit errors. Without gray coding, such an error could corrupt both bits of a symbol and result in doubling the BER. A Gray-coded QPSK constellation is shown in Figure 3.1, where each adjacent constellation point differs by at most one bit.

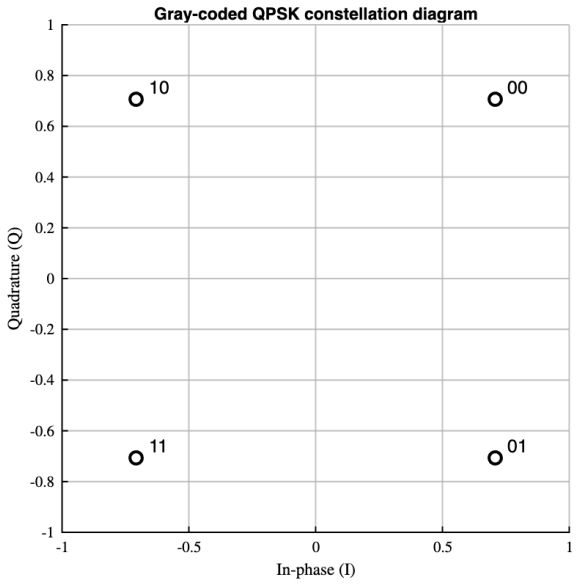

Figure 3.1: Gray-coded constellation diagram of QPSK.

3.2 Pulse shaping and root raised cosine filter

In single carrier systems, pulse shaping is used to create a waveform of the modulated symbols that has controlled spectral characteristics and reduced intersymbol interference (ISI). Instead of transmitting ideal impulses for each symbol, each symbol is shaped by a pulse with finite duration. This allows the signal to occupy a well-defined bandwidth and limits out-of-band emissions [7].

A common pulse shaping filter used in single-carrier systems is a root-raised-cosine filter (RRC) at the transmitter. RRC filters fulfill the Nyquist criterion, which states that a filter's impulse response must be zero at all neighboring symbols, ensuring that symbols do not interfere with each other at the receiver. RRC filters also allow for modification of how much excess bandwidth is used beyond the minimum required bandwidth. This is achieved by changing the roll-off factor (α). α describes how steep the edges of the pulse are in the frequency domain, and consequently how large the side lobes of the pulse are in the time domain [9], as depicted in Figure 3.2. The passband bandwidth of the RRC filter can be expressed as

$$W = \frac{1+\alpha}{T}. \tag{3.2}$$

Larger values of α make the system less sensitive to timing errors but also increase the signal's occupied bandwidth (OBW) as described in Equation (3.2). The value of α can therefore be described as excess bandwidth. When applying matched filtering with an RRC pulse x_{rrc}, a matched RRC pulse can be convolved at the receiver end to achieve a matched filter [14], [15]. This results in a raised-cosine pulse.

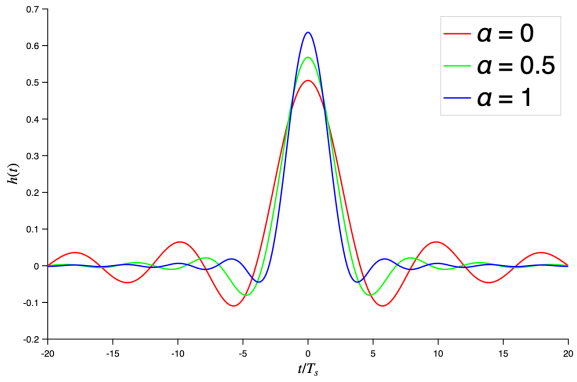

Figure 3.2: Impulse responses of the root-raised cosine filter for roll-off factors $\alpha = 0$ (red), $\alpha = 0.5$ (green), and $\alpha = 1$ (blue). The horizontal axis represents the normalized time index, and the vertical axis shows the filter impulse response $h(t)$.

3.3 Metrics and visual tools in digital communications

In digital communication systems, evaluating performance is essential to understand how efficiently and reliably information is transmitted over a channel. Different metrics are used to capture various aspects of system behavior, such as data rate efficiency, error probability, and signal quality. Rather than relying on a single measure, a combination of complementary metrics provides a more complete picture of system performance under different conditions.

One important aspect is how effectively the available resources are utilized, which is typically quantified in terms of throughput. The throughput of a system can be expressed as

$$R_{\text{throughput}} = \frac{n_f - n_o}{n_f} \times R_s \times \log_2(M) \times p_{\text{success}}, \tag{3.3}$$

where n_o is the number of overhead bits and n_f is the total number of bits in the transmitted frame. Further, the success rate $p_{success}$ is defined as the ratio between correctly received bits and the total number of transmitted bits. $R_s \log_2(M)$ is the data rate of the system, where R_s is the symbol rate in symbols per second.

The frame duration is defined as

$$t_f = \frac{N_{sym}}{R_s}, \tag{3.4}$$

where N_{sym} denotes the total number of symbols in a frame.

BER is a key performance metric in digital communication systems that quantifies how often transmitted bits are incorrectly received. For empirical measurements, BER is defined as the ratio between the number of incorrectly detected bits and the total number of transmitted bits, expressed as

$$\text{BER} = \frac{N_{\text{err}}}{N_{\text{bits}}}, \tag{3.5}$$

where N_{err} denotes the number of erroneous bits and N_{bits} represents the total number of transmitted bits.

Another important metric in digital communication systems is EVM, which is a measure of the difference between ideal transmitted constellation points and their received estimates. It reflects how distortion or noise affects the signal quality, with lower values indicating better system performance and more accurate symbol transmission. Root mean square EVM is defined as

$$\text{EVM} = \sqrt{\frac{\sum_{k=1}^{N} |a_k - \hat{a}_k|^2}{\sum_{k=1}^{N} |a_k|^2}} \times 100. \tag{3.6}$$

The parameter N denotes the total number of transmitted symbols, a_k represents the k-th transmitted (true) symbol, and $\hat{a}_k$ denotes the corresponding estimated symbol according to Equation (3.1) [16]. The EVM is commonly expressed as a percentage, which is why the expression in Equation (3.6) is multiplied by 100.

In addition, there are other visual tools that can be used to identify issues or distortions in communication systems. One such tool is the eye diagram, visualized in Figure 3.3. Although it does not provide explicit numerical metrics, it provides a visual examination of the severity of ISI, noise, and sensitivity to timing errors [17]. The best time to sample the received signal is when the eye is open the widest. The width of the central eye opening indicates the time interval over which the received signal can be sampled without experiencing ISI. In the absence of ISI, the eye is fully open, corresponding to a normalized opening of one. As ISI increases, the eye gradually closes, and in the extreme case of severe ISI, the eye opening reduces to zero [17].

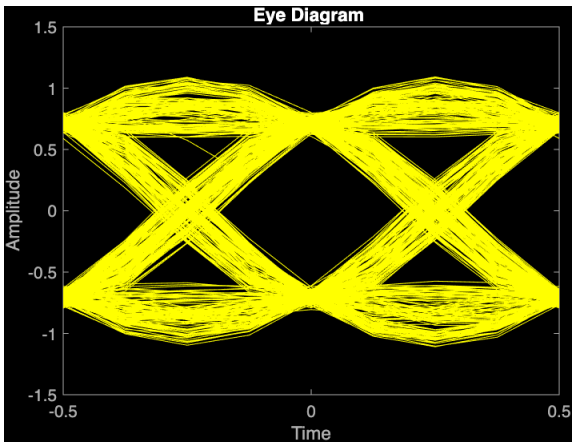

Figure 3.3: In-phase channel eye diagram with roll-off factor, $\alpha = 0.5$.

3.4 Synchronization and preambles

A preamble is a sequence of symbols that is known by both the receiver and the transmitter in a communication system. Preambles are used for various purposes, but their primary function is to enable the receiver to detect the signal and estimate the effects the transmitted symbols experience.

PN sequences

One widely used type of preamble is based on pseudorandom noise (PN) sequences. A PN sequence is a binary sequence that is generated and has properties resembling random noise. A well-chosen PN sequence has an autocorrelation function that produces a sharp peak at zero lag and low values everywhere else [18]. The strong autocorrelation properties of the sequence make it possible for the receiver to locate it within a noisy received signal. The correlation output spikes when the known sequence matches the received copy and stays low otherwise [19].

The length of the PN sequence involves a trade-off between detection reliability and transmission overhead. A longer sequence gives a more prominent correlation peak, which makes detection more reliable. However, a longer preamble occupies a larger portion of the transmitted frame, leaving less space available for the payload data [20]. In addition, longer preambles reduce the overall system throughput, as shown in Equation (3.3). This reduction is caused by the increased overhead, where overhead refers to transmission resources that are not used for transmitting actual information data. Therefore, the choice of sequence length depends on the channel conditions and the amount of overhead the system can tolerate.

Frame synchronization

Preambles can be used to find the boundaries of a transmitted frame by cross-correlating the received signal with a known preamble sequence [21]. A preamble used for timing estimation does not contain periodic structures, as repeating patterns can cause the receiver to lock onto an incorrect timing position. Therefore, sequences with strong autocorrelation properties, such as PN sequences, are often preferred for frame synchronization. Low-order modulation schemes such as binary phase shift keying (BPSK) are well-suited for preamble symbols due to their robustness and reliable detection performance. BPSK is a simplified form of phase shift keying in which each symbol represents a single bit. In this scheme, a binary 0 is mapped to a signal amplitude of -1, while a binary 1 is mapped to a signal amplitude of +1. As illustrated in Figure 3.4, a PN-sequence has a strong autocorrelation peak only at zero lag with significantly suppressed sidelobes.

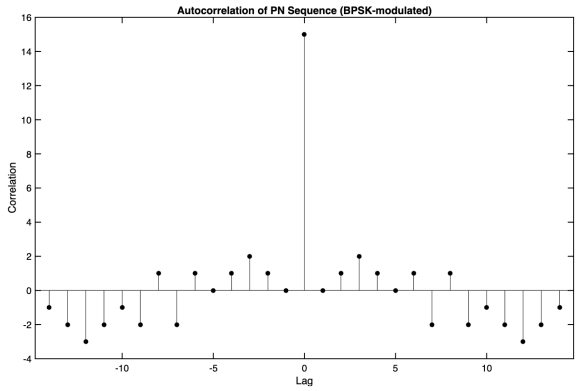

Figure 3.4: Autocorrelation of a BPSK modulated PN sequence.

Phase synchronization

As illustrated and presented in Section 2.2, a phase offset appears as a constant phase rotation of the received constellation. Consequently, the phase offset can be estimated and compensated for using a known preamble.

$$\hat{\phi} = \arg(P_r \cdot P_t^*), \tag{3.7}$$

where P_r is the received preamble, and P_t^* is the conjugate transmitted preamble known at the receiver, $arg(.)$ denotes the argument, the phase angle, of a complex number.

CFO synchronization

There are many methods for estimating CFO, and these estimators are generally classified into two categories: data-aided and non-data-aided (blind) techniques [22]. However, this project will only focus on data-aided techniques where known reference signals are exploited to facilitate synchronization. Preambles are commonly used to estimate CFO in practical communication systems. A widely used approach is to transmit a repeated preamble, forming two halves r_1 and r_2 with lengths L. The repetitive preamble is useful for estimating the CFO by utilizing the autocorrelation of the received preamble [22]. Consequently, the fractional CFO can be estimated

$$\hat{\epsilon} = \frac{1}{2\pi L} \sum_{n=0}^{L-1} \arg(r_2[n] \times r_1^*[n]). \tag{3.8}$$

In the absence of the CFO, the halves r_1 and r_2 are identical in phase. However, if a CFO is present, a phase shift occurs between the halves. As shown in Equation (2.3), the CFO introduces a linear phase rotation over time. Consequently, by measuring the phase difference between the two received halves, the receiver can estimate the accumulated phase shift, which is directly proportional to the CFO. In general, using a larger number of samples improves the accuracy and robustness of the estimate by reducing the impact of noise. However, this comes at the cost of increased preamble overhead, creating a trade-off between estimation performance and spectral efficiency when selecting the preamble length.

3.5 Maximum ratio combining

In MIMO systems, the uplink transmission is received independently at multiple RRHs, each of which captures a different version of the signal due to its own channel conditions. Modern MIMO architectures exploit this spatial diversity by combining the received signals to improve overall performance. The received signals at each RRH can be combined using maximum ratio combining (MRC), which maximizes the output SNR by coherently aggregating the energy from all received antenna streams [23]. The per-antenna received signal is defined in the system model in Section 2.4. If a known preamble is embedded in the transmitted frame, channel estimation can be applied to estimate each channel gain and its corresponding phase. The least-squares estimate of the channel gain is

$$\hat{h}_i = \frac{\sum_{k=1}^{N} P_t^*[k]\, P_r[k]}{\sum_{k=1}^{N} |P_t[k]|^2} \tag{3.9}$$

where P_r is the received preamble, P_t is the transmitted preamble symbols known at the receiver, and N is the number of preamble symbols used for the channel estimation.

The optimal MRC output signal can then be estimated [24]

$$z = \sum_{i=1}^{N_r} \hat{h}_i^* r_i, \tag{3.10}$$

where z is the MRC output signal, $\hat{h}_i^*$ is the conjugated least-square estimate of the channel gain, r_i is the received baseband signal at antenna i, and N_r is the number of receiving antennas.

4

Methodology

This chapter presents the experimental methodology used to design, implement, and evaluate the USRP-based user equipment. The work is structured into two main development phases.

The first phase involves developing and optimizing software to enable reliable communication between two USRP devices. During this stage, the system is pushed to its operational limits to determine the maximum achievable bandwidth, throughput, and signal duration.

The second phase focuses on integrating the system into the D-MIMO testbed. This includes estimating and compensating for the CFO without relying on external reference signals. Furthermore, experiments are conducted within the Chalmers testbed environment, where MRC is implemented to coherently combine received signals.

4.1 Software implementation and verification

The system was implemented in MATLAB using the UHD drivers together with the Communications Toolbox Support Package for USRP Radio, which provided control of the USRP devices. The code was stored in a Git repository on GitHub to enable collaboration and version control.

The project used an iterative development approach. Each module of the system was developed individually and tested frequently. If problems appeared during the experiment, they were fixed in the software before being tested again. The same approach was used when testing the entire system.

The system modules were tested by sending test data to each module and examining the results. Because each module was validated individually, coding errors could be identified and corrected more efficiently, since the source of an error could be localized more easily than if the entire system were tested simultaneously.

If the modules did not perform as expected, they were systematically debugged by further analysis. Intermediate variables were logged and visualized, and the code was reviewed to identify potential issues. In this step, MATLAB visualization tools

such as constellation plots, spectrum analyzers, and eye diagrams were extensively utilized.

A simulation channel was also implemented to facilitate the development. The simulation channel was designed to operate according to the signal model described in Equation (2.5). Instead of transmitting the symbols via cable or antenna, they were sent via a simulation channel in MATLAB. The channel supported simulation for the signal distortions described in Section 2.2.

4.2 Point-to-point USRP communication

The experimental methodology follows a staged approach, where the USRP is first verified to have functional transmitting and receiving chains, both over cable and through a wireless link. Once this is confirmed, full USRP-to-USRP communication is established. An overview of the hardware specifications for the USRP B205mini-i is provided in Appendix B.

Communication via cable

Figure 4.1 illustrates the experimental setup used to verify the receiving capabilities of the USRP through a coaxial cable. In this phase, a function generator is used to transmit a predetermined waveform through the coaxial cable to the USRP receive port. The setup also includes MATLAB-based processing to verify the correctness of the received signal.

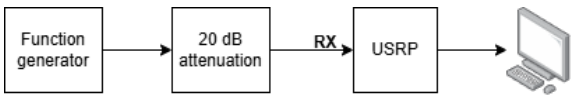

Figure 4.1: Experimental setup for verifying the receiving capabilities via cable.

After validating the receiving capabilities of the USRP, experiments are conducted to evaluate its transmitting performance. As shown in Figure 4.2, the USRP is connected to an oscilloscope through the coaxial cable. The transmitted signal is then verified using the oscilloscope. Due to potential limitations of the oscilloscope, such as bandwidth and sampling rate, a lower frequency than 2.35 GHz was used during initial testing. In this case, a signal with a carrier frequency of 100 MHz was selected to ensure reliable measurement within the oscilloscope's operational limits [25]. When measuring the transmitted signal, a 30 dB attenuator was connected between the transmitter output and the oscilloscope input to reduce the signal power and prevent damage to any equipment.

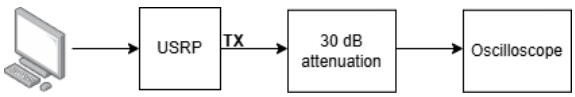

Figure 4.2: Experimental setup for verifying the transmitting capabilities via cable.

Wired link

Once wired transmission and reception had been verified, half-duplex communication between the USRPs was established. As illustrated in Figure 4.3, the USRPs were connected to the same host computer. The devices were interconnected through a cable and a 10 dB attenuator to limit the received power. In addition, both USRPs were connected to a common 10 MHz reference signal to provide a shared reference for the LOs. In this phase, QPSK modulation was implemented in MATLAB using the Communications Toolbox to generate a baseband signal from randomly generated bits. After modulation, upsampling and pulse shaping were performed. The USRP hardware then upconverted the baseband signal to the desired carrier frequency before transmission. As illustrated in Figure 4.4, the transmitted baseband signal consisted of two parts, forming the frame structure: a PN sequence and payload bits. Once the implementation had been successfully verified, the signal quality was evaluated using the metrics described in Section 3.3.

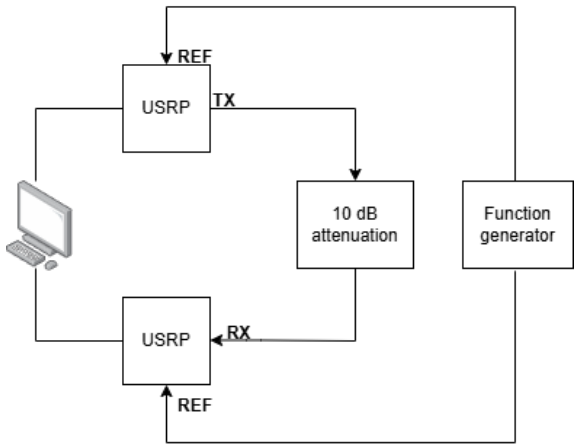

Figure 4.3: Experimental setup for evaluating wired USRP-to-USRP communication.

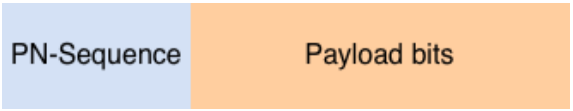

Figure 4.4: Frame structure with PN-sequence preamble. The number of payload bits is arbitrary.

Wireless link

After establishing a wired link with satisfactory performance, a wireless link between the USRPs was implemented and subsequently optimized. As illustrated in Figure 4.5, the carrier frequency was configured to 2.35 GHz, which corresponds to the operating frequency of the D-MIMO testbed.

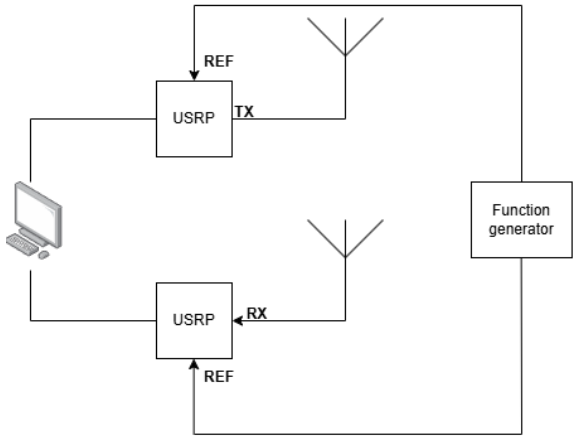

Figure 4.5: Experimental setup for evaluating full wireless USRP-to-USRP communication.

4.3 Experimental evaluation methodology

PN-sequence optimization

To reduce the number of overhead bits for the frame synchronization preamble, four PN sequences with different lengths were tested over the wireless channel. The tested PN sequences had lengths of 3 bits, 7 bits, 15 bits, and 31 bits. Each sequence length was evaluated across 10 trials, where the correlation peak, BER, and EVM of each transmission were recorded. All transmissions were conducted using 1000 payload symbols.

Maximum usable signal bandwidth

The transmitted signal bandwidth is defined in terms of occupied bandwidth, specifically for a RRC passband signal with roll-off factor α, as defined in Equation (3.2). In practice, the OBW is commonly quantified using the 99% occupied bandwidth metric, which is defined as the frequency interval containing 99% of the total signal power. This definition is widely adopted because it provides a robust and reproducible estimate of the effective signal bandwidth. By excluding only the outermost spectral components, which typically contain negligible power and noise contributions, the 99% OBW provides a stable and reliable measure of the signal bandwidth.

At the transmitting USRP, the digital IQ samples are converted into an analog waveform by a DAC. Before digital-to-analog conversion, interpolation is applied to insert additional samples between consecutive baseband samples. This process effectively lowers the symbol rate relative to the DAC sampling rate. Consequently, the effective transmit sampling rate at the DAC is given by

$$f_s = \frac{R_c}{L}, \tag{4.1}$$

where R_c denotes the master clock rate and L is the interpolation factor. As L

increases, the effective sampling rate decreases, resulting in a larger time interval between consecutive transmitted samples.

In order to maximize the occupied bandwidth, the interpolation factor was set to 1, and N_s was set to 2. To evaluate the maximum usable signal bandwidth, the master clock rate was incremented in steps from 32, 42, 56, and 61.44 MHz, which increases the sample rate according to Equation (4.1). At each step, five frames consisting of 10000 bits were transmitted and received, and both BER and EVM were measured. The largest OBW at which the BER remains below 10^{-3} was reported as the maximum usable signal bandwidth.

Maximum achievable throughput

To determine the maximum achievable throughput in bits per second, a roll-off factor sweep experiment was performed. The symbol rate is defined as:

$$R_s = \frac{f_s}{N_s} = \frac{1}{T_s N_s}, \tag{4.2}$$

where f_s is the sample rate and N_s is the number of samples per symbol. Equation (3.2) can be rewritten to extract R_s

$$R_s = \frac{W}{1+\alpha}. \tag{4.3}$$

The N_s is held constant at 2, while the master clock rate R_c was held at 61.44 MHz, which is the maximum clock rate. The roll-off factor, α, was swept from 0.1 to 0.5, incrementing in steps of 0.1. Five frames consisting of 10000 bits were transmitted and received for each step, and the BER and EVM were computed. The observed bandwidth that contains 99% of the transmitted signal power was first computed. The corresponding symbol rate was then computed using Equation (4.3). Consequently, the throughput could be computed according to Equation (3.3). The highest $R_{throughput}$ at which the BER stays below 10^{-3}, corresponding to achieving a success rate of at least 99.9% was recorded as the maximum throughput.

Maximum signal duration

To evaluate the maximum signal duration, frames of varying lengths were transmitted. To determine the longest successfully transmittable frame, increasingly larger frames ranging from 1000 to 50000 symbols were transmitted. Each frame length was transmitted five times, and the BER and EVM were recorded. For each frame length, the 99% OBW of the signal was computed and used to compute the symbol rate according to Equation (4.3). With the symbol rate computed, the corresponding signal duration was computed according to Equation (3.4).

CFO estimation

To enable the USRPs to function as flexible user equipment, it was desirable to operate them without relying on external references from a function generator. To estimate the CFO without external references, a second preamble was introduced. The second preamble consisted of a randomized sequence repeated once, as illustrated in Figure 4.6. This repetition enables estimation of the CFO according to Equation (3.8).

To optimize both overhead bits and estimation performance, five different preamble lengths were tested. Each preamble length was tested using transmissions containing 10000 symbols, as this sample size made the effects of CFO clearly observable. The tested preamble lengths were 32, 64, 128, 256, and 512 bits modulated using BPSK. For each case, the BER and EVM were recorded.

It was also of interest to evaluate whether estimating the CFO at the very first transmission after powering up the USRP was sufficient. To investigate this, two tests were conducted. In the first test, data were continuously transmitted to the receiving USRP while estimating the CFO over an extended period to observe how it varied over time. The second test followed the same procedure but began after the USRP had been powered on for a longer duration to investigate if the CFO saturates when the USRP reached a stable operating temperature.

Figure 4.6: Frame structure used for CFO estimation. The CFO preamble consists of two identical halves.

4.4 Integration into D-MIMO testbed

To evaluate the proposed system within the D-MIMO testbed, the USRP-based user equipment was integrated into the experimental setup. The USRP was connected to a centrally located antenna via an SMA cable, enabling wireless transmission within the testbed environment. During the measurements, each user signal was transmitted from the USRP and independently received at the six RRHs. The transmitted frames consisted of a 15-bit PN sequence, a 128-bit CFO estimation preamble, and 500 payload symbols. The lengths of the payload and CFO preamble sequences were constrained to 500 and 128 symbols, respectively, to remain within the FPGAs on-board memory limitations. As described in Section 2.4, the testbed supports a maximum receive signal duration of 76.8 μs, which imposes a strict constraint on frame design. To maximize the number of transmitted symbols while still accommodating the required preamble overhead, the master clock rate R_c was configured to its maximum value of 61.44 MHz. In addition, the interpolation factor was set to 1 to maximize the transmit sampling rate of the USRP, as defined in Equation (4.1). Based on these settings, the maximum number of symbols that could be reliably

transmitted within a single frame was determined. The transmitted signal occupied a bandwidth of 19.3 MHz. Using Equation (4.3), the corresponding symbol rate was computed, and Equation (3.4) was then used to determine the maximum number of symbols that could be transmitted within the available time window. For a signal bandwidth of 19.3 MHz and roll-off factor $\alpha = 0.5$, the maximum supported frame length was computed to be 995 symbols, including both preamble and payload symbols. However, to ensure reliable reception, the frame duration t_f should satisfy $t_f \leq t_{f,max}/2$. Consequently, the transmitted frame contains significantly fewer symbols than the maximum number supported by the testbed.

At the receiver side, the baseband signals were forwarded to the FPGA, where they were time-aligned and combined to emulate a D-MIMO uplink scenario. The signals from the six RRHs were combined using MRC, as defined in Equation (3.10). The channel gains were estimated using the received CFO preamble and the corresponding known transmitted CFO preamble. The resulting MRC output served as a reference for comparison with the signals received individually at each RRH.

For each transmission attempt, system performance was evaluated using standard metrics derived from the demodulated data. In particular, the EVM was computed to assess modulation accuracy, while the BER was used to quantify the reliability of the received bitstream.

5

Experimental Results

This chapter presents the experimental results from the conducted experiments. The experiments cover frame synchronization, preamble length, maximum throughput, signal bandwidth, signal duration, CFO estimation, and integration into the D-MIMO testbed using MRC.

5.1 Parameter values for wireless communication

Table 5.1: USRP settings.

Wireless system	
Carrier frequency	2.35 GHz
Tx gain	51 dB
Rx gain	38 dB
Master clock rate	32 MHz
Interpolation factor	2
Decimation factor	2

Table 5.2: Standard RRC filter parameters.

Filter parameters	
α	0.5
N_s	4
Filter span	10

Table 5.3: Standard parameters for wireless experiments.

Experimental setup parameters	
Distance between antennas	0.5 m
Transmit power	9 dBm
Sample rate	16 MHz

The USRP settings shown in Table 5.1, filter parameters shown in Table 5.2, and the experiment parameters shown in Table 5.3 are used in the upcoming tests if nothing else is specified.

5.2 Synchronization performance

PN-sequence

Below are the results from the frame synchronization test to optimize the PN sequence length. Each PN-sequence was evaluated under 10 trials.

Table 5.4: EVM, BER, and correlation peaks from varying lengths of PN-sequences.

PN-sequence length [bits]	BER	EVM [%]	Correlation peak
3	0.5101	145.93	0.0518
7	0	9.47	0.1116
15	0	7.63	0.2482
31	0	7.73	0.5655

As shown in Table 5.4, the 15-bit PN sequence provides the best performance by yielding the lowest overhead. Therefore, the 15-bit PN sequence is selected for frame synchronization and will be used in the upcoming tests.

CFO estimation

In the CFO estimation results, all measurements were obtained without the use of external references. Each test was conducted using 10000 symbols across five trials for each preamble length.

Table 5.5: BER and EVM for different CFO preamble length.

Preamble length [bits]	BER	EVM [%]
32	0.2842	98.28
64	0.0110	25.35
128	0	18.55
256	0	12.13
512	0	8.03

As can be seen in Table 5.5, the BER and EVM decrease when increasing the preamble length. This result is expected since larger preambles improve the averaging process and reduce the influence of noise on the CFO estimation.

As can be seen in Figure 5.3, the constellation without CFO correction results in a heavily rotated constellation, where the constellation clusters are nonexistent. In

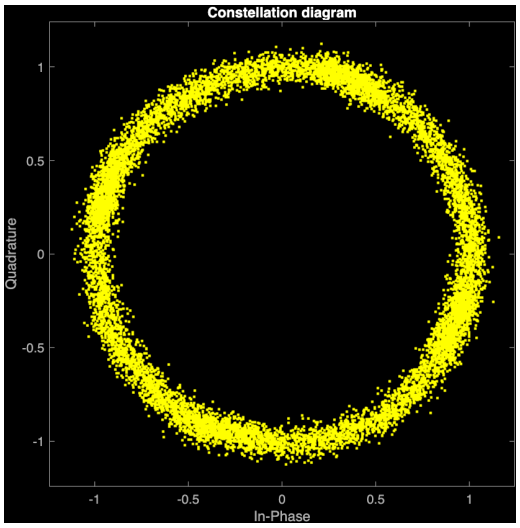

(a) Constellation without CFO correction.

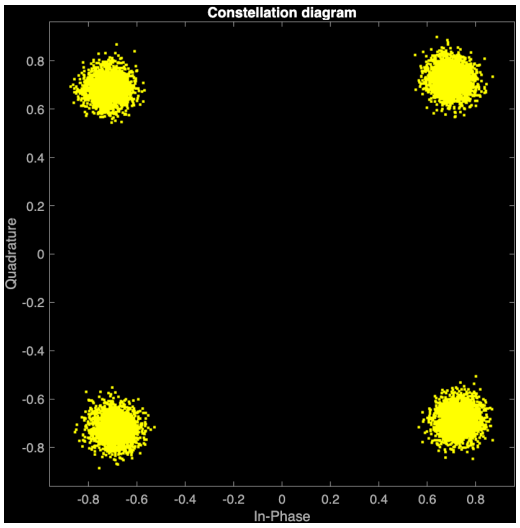

(b) Constellation with CFO correction using 512-bit preamble.

Figure 5.1: Effect of CFO correction on constellation quality.

contrast, applying CFO correction using a 512-bit preamble results in the received constellation forming four distinct clusters.

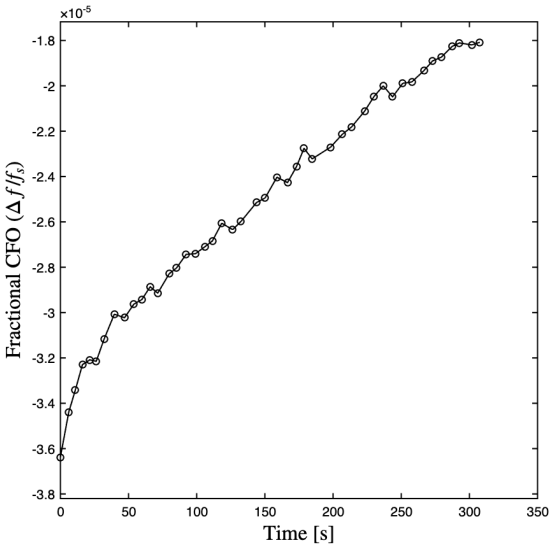

(a) Measured variation of fractional CFO over time starting from initialization of USRP.

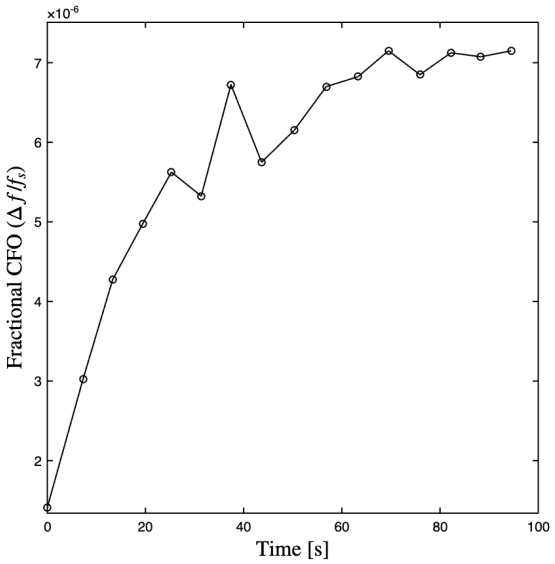

(b) Measured variation of fractional CFO over time during long-term operation of the USRP.

Figure 5.2: Measured fractional CFO over time.

Figure 5.2a shows the CFO from the initial start-up of the transmitter. A significant increase in the fractional CFO can be observed during this period. Figure 5.2b illustrates the long-term variation of the fractional CFO after continuous USRP operation. The CFO initially increases rapidly after start-up, but its variations

gradually stabilize over time as the system reaches a steady state.

5.3 Results on maximum throughput and signal bandwidth

Below are the results of the throughput and signal bandwidth test to optimize the value of the roll-off factor α and master clock rate R_c.

Table 5.6: Achieved bandwidth and throughput from varying roll-off factor from 0.1 to 0.5, N_s set to 2, and R_c to 61.44 MHz.

α	$P_{success}$ [%]	EVM [%]	OBW [MHz]	R_s [Msym/s]	$R_{throughput}$ [Mbit/s]
0.1	90.82	26.99	31.47	28.61	51.89
0.2	99.97	20.79	32.61	27.18	54.25
0.3	99.97	24.17	34.41	26.47	52.84
0.4	100	15.70	36.33	25.95	51.82
0.5	100	12.60	38.45	25.63	51.19

Table 5.6 shows the achieved bandwidth and throughput for roll-off factors ranging from 0.1 to 0.5. The highest achievable throughput is 54.25 Mbit/s for $\alpha = 0.2$, corresponding to a success rate above 99.9%.

It is also observed that decreasing the roll-off factor α degrades both EVM and success rate performance. Constellation diagrams show increased symbol dispersion and the formation of bridges between adjacent symbols, indicating higher ISI. Based on this observation, eye diagrams of the received samples were plotted for $\alpha = 0.1$ and $\alpha = 0.4$. The case $\alpha = 0.1$ shows pronounced ISI, while $\alpha = 0.4$ exhibits no visible ISI-related errors.

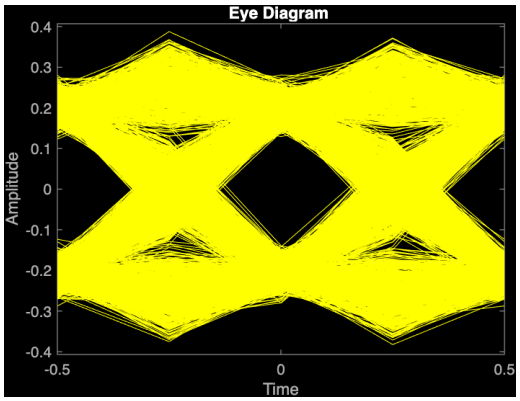

(a) Eye diagram of received samples during throughput test with $\alpha = 0.4$.

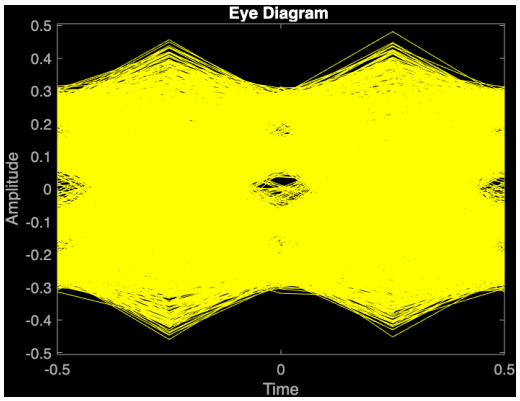

(b) Eye diagram of received samples during throughput test with $\alpha = 0.1$.

Figure 5.3: Comparison of eye diagrams for $\alpha = 0.1$ and $\alpha = 0.4$, illustrating the effect of ISI on the received signal.

Table 5.7: OBW, EVM, and BER achieved by varying the master clock rate R_c. N_s set to 2 and $\alpha = 1$.

R_c [MHz]	BER	EVM [%]	OBW [MHz]
32	0	9.24	25.80
48	0	11.14	38.63
56	0	11.60	45.11
61.44	0	11.10	49.51

Table 5.7 shows the results of the maximum usable bandwidth test, where the master clock rate R_c was swept from 32 to 61.44 MHz. The results show that increasing the clock rate, and consequently the sample rate, increases the occupied bandwidth. By applying the constraint BER $\leq 10^{-3}$, the maximum usable clock rate is determined to be 61.44 MHz, corresponding to a signal bandwidth of 49.51 MHz.

5.4 Results on signal duration

The results from the signal duration are presented below, where the number of transmitted symbols was swept from 1000 to 50000 symbols.

Table 5.8: Symbol rate, EVM, and frame transmission time from the signal duration test. Frame length varies from 1000 symbols to 50000 symbols.

Nr. symbols	BER	EVM [%]	R_s [Msym/s]	t_f [ms]
1000	0	6.27	3.38	0.296
2000	0	7.11	3.38	0.592
3000	0	8.90	3.38	0.888
5000	0	9.44	3.36	1.490
10000	0	11.17	3.38	2.968
20000	0	13.62	3.38	5.917
30000	0	15.31	3.38	8.902
40000	0	14.49	3.38	11.852
50000	0	14.48	3.38	14.836

As can be seen in Table 5.8, increasing the number of transmitted symbols leads to a higher EVM. However, the BER remains 0 in all cases. This indicates that transmitting a larger number of symbols does not introduce any practical limitations for the USRPs under the tested conditions.

In addition, Table 5.8 shows that the computed symbol rate remains constant for frame lengths ranging from 1000 to 50000 symbols. Consequently, the frame duration increases proportionally with the frame length.

To verify the accuracy of the computed frame duration, a frame containing 50000 symbols was transmitted and measured using an oscilloscope. Figure 5.4 illustrates

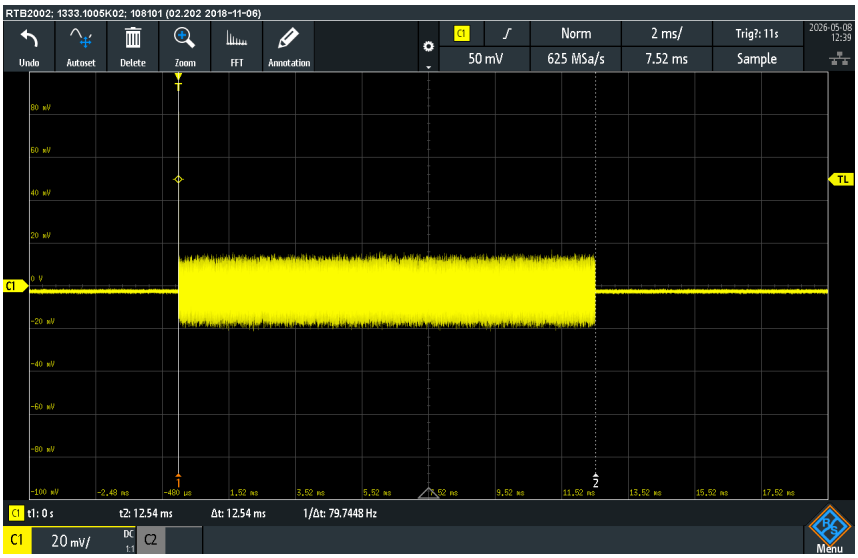

Figure 5.4: Measured signal duration of 50000 symbols with oscilloscope.

the received frame, where the frame duration was measured to be 12.54 ms. This corresponds to a deviation of 2.3 ms compared to the computed frame duration for 50000 symbols in Table 5.8.

5.5 D-MIMO testbed experimental results

Below are the results from one of the transmission tests to the D-MIMO testbed at Chalmers.

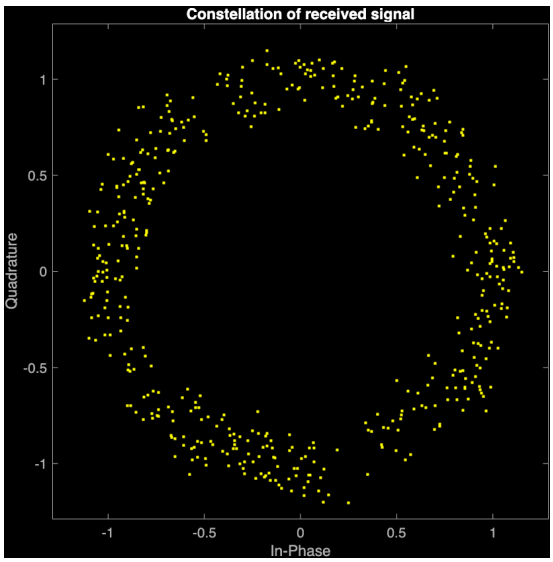

(a) Constellation without CFO correction. BER and EVM computed to 0.212 and 79.99%, respectively.

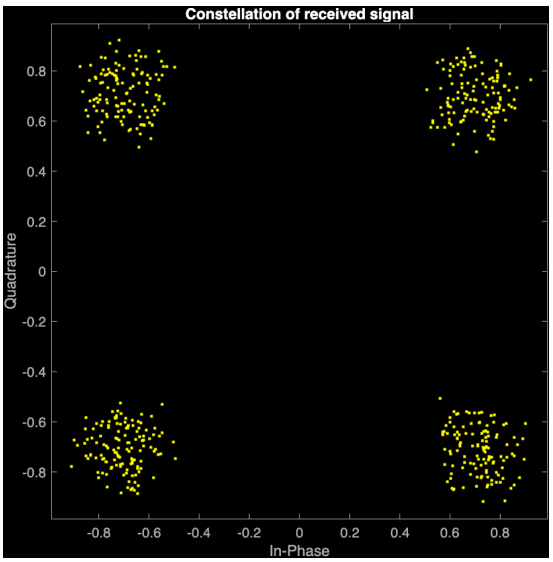

(b) Constellation with CFO correction using 128-bit preamble. BER and EVM computed to 0 and 12.61%, respectively.

Figure 5.5: Constellation diagrams obtained from the testbed: (a) without CFO correction and (b) with CFO correction.

Figure 5.5a shows the constellation diagrams obtained from the testbed without CFO correction, and with CFO correction, which can be seen in Figure 5.5b. As shown in Figure 5.5a, the CFO between the USRP and the testbed LOs is significant, resulting in a clearly rotating constellation even for a payload consisting of only 500 symbols. However, the 128-bit preamble is capable of accurately estimating and compensating for the CFO, as illustrated in Figure 5.5b.

Table 5.9: Achieved BER and EVM from testbed experiments. Metrics are presented for each RRH separately and for the combined MRC estimate across all RRHs.

RRH #	1	2	3	4	5	6	MRC
BER	0	0	0	0	0	0	0
EVM	20.07%	12.61%	24.17%	15.22%	14.53%	14.24%	4.64%

Table 5.9 presents the computed BER and EVM for each RRH individually, as well as for the combined MRC estimate across all RRHs. While the individual RRHs exhibit significantly different EVM values, the BER remains constant at zero for all cases. This variation in EVM is caused by the different channel conditions

experienced by each RRH. By combining the received signals using MRC, the overall EVM is improved to 4.64%.

6

Discussion

This chapter discusses the findings of the experiment conducted on the USRP-based communication system. Possible explanations for the observed results and the trade-offs involved in the system design will also be presented.

6.1 Communication performance

The parameter settings presented in Tables 5.1 and 5.2 establish a stable operating point for all subsequent wireless experiments and define the baseline conditions of the system. The transmit and receive gains presented in Table 5.1 were selected to ensure sufficient received signal strength while avoiding saturation of the receiver front-end amplifiers.

The obtained results demonstrate a highly reliable communication system with stable performance throughout the conducted experiments for both BER and EVM. However, this high reliability may also indicate that the system was not operating within its performance limits. The experiments were performed under relatively favorable conditions, including a line-of-sight propagation channel and the use of a relatively low modulation order, both of which reduce the likelihood of transmission errors. Consequently, the evaluated scenario may not fully reflect the challenges encountered in more demanding wireless environments, such as severe multipath propagation, non-line-of-sight conditions, or higher-order modulation schemes that are more sensitive to noise and channel impairments [26]. Therefore, the obtained results should primarily be interpreted as a proof-of-concept under controlled laboratory conditions rather than as a characterization of performance in practical large-scale deployment scenarios.

6.2 Synchronization challenges

As shown in Table 5.4, longer PN sequences produce higher cross-correlation peaks. However, the usefulness of the correlation peak values can be questioned since the increase in peak magnitude is inherently tied to the sequence length rather than indicating improved detection performance. On the other hand, increasing the length of the PN sequence improves system performance in terms of both BER and EVM.

With a 3-bit PN sequence, the system tends to lock onto incorrect indices, resulting in failed detection of the correct frame boundaries. In contrast, a 7-bit PN sequence consistently detects the correct frame boundaries. This demonstrates the importance of selecting a sufficiently long synchronization sequence to ensure robust frame detection while simultaneously minimizing unnecessary transmission overhead. However, it still provides a limited number of samples, which is insufficient for accurately estimating the phase offset between the transmitter and receiver.

In Table 5.5, increasing the preamble length leads to lower BER and EVM. This is expected, as a longer preamble provides more samples for CFO estimation, improving robustness in the presence of noise. However, this improvement comes at the cost of increased overhead, which reduces the overall system throughput.

A similar trend is observed in the simulated results presented in Appendix A, where both BER and EVM decrease with increasing preamble length. However, the simulated values are consistently higher than those measured in the real system for the same preamble lengths. This discrepancy is likely due to different SNR conditions, suggesting that the experimental setup operated under more favorable channel conditions than those assumed in the simulations.

Regarding the choice of preamble length, a clear performance transition is observed between 64 and 128 bits. Below 128 bits, the CFO estimation is insufficiently accurate, resulting in non-zero BER. From 128 bits and above, the BER drops to zero, while the EVM continues to improve with increasing preamble length. Beyond this point, the choice of preamble length (e.g., 128, 256, or 512 bits) becomes a trade-off between additional performance gain in EVM and increased overhead.

Furthermore, it is shown in Figure 5.2 that the fractional CFO between the USRPs seems to increase if the transmitter is continuously active. This is likely due to temperature-induced drift in the LO, caused by heat generated in the circuit during operation [27]. However, it does seem to saturate if active for a longer period of time. This indicates that the oscillator frequency stabilizes as the hardware approaches thermal equilibrium. Consequently, the CFO becomes more predictable after prolonged operation, improving the reliability of the CFO estimation process. The results also demonstrate an important tradeoff between synchronization robustness and spectral efficiency. While longer synchronization preambles improve estimation accuracy and reduce BER and EVM, they simultaneously increase transmission overhead and reduce the achievable throughput.

6.3 Throughput vs reliability tradeoffs

The results presented in Table 5.6 demonstrate that the roll-off factor has a significant influence on both OBW and the overall communication performance. The OBW increases from 31.47 MHz at a roll-off factor of 0.1 to 38.45 MHz at a roll-off factor of 0.5. This behavior is consistent with Equation (3.2), where a larger roll-off factor increases the excess bandwidth introduced by the pulse-shaping filter. At the

same time, increasing the roll-off factor improves the signal quality, as reflected by both the success rate and the EVM. The success rate increases from 90.82% at a roll-off factor of 0.1 to 100% at roll-off factors of 0.4 and 0.5, while the EVM decreases from 26.99% to 12.60%. This improvement is likely caused by reduced ISI and increased tolerance to timing errors. Larger roll-off factors produce pulses with smaller time-domain side lobes, which reduces symbol interference and improves symbol detection reliability.

This behavior becomes particularly visible in the eye diagrams presented in Figure 5.3b and Figure 5.3a. For the larger roll-off factor, the eye opening is significantly wider, indicating that the received signal can be sampled with reduced sensitivity to timing errors and ISI. In contrast, the eye diagram corresponding to $\alpha = 0.1$ is nearly closed, demonstrating that the available sampling interval without ISI becomes considerably smaller.

Despite the large differences in EVM and success rate in Table 5.6, the throughput remains relatively stable for all tested roll-off factors and varies between approximately 51 and 54 Mbit/s. The highest throughput is achieved at a roll-off factor of 0.2, resulting in a throughput of 54.25 Mbit/s. This demonstrates that the highest throughput does not necessarily coincide with the best EVM or success rate. Instead, the throughput depends not only on the symbol rate, but also on the received success rate, as shown in Equation (3.3). However, if comparable performance can be maintained with a higher modulation order, the achievable maximum throughput can be significantly increased.

Furthermore, Equation (3.2) shows that increasing the roll-off factor reduces the achievable symbol rate for a fixed bandwidth. Consequently, the selection of roll-off factor represents a tradeoff between spectral efficiency and signal quality. Under the tested conditions, $\alpha = 0.2$ provided the highest throughput while still maintaining reliable communication performance with a success rate of 99.97%.

Overall, Table 5.6 shows that larger roll-off factors improve both the success rate and the EVM. However, these improvements come at the cost of increased OBW and reduced symbol rate, while the throughput remains relatively unchanged. The choice of roll-off factor therefore represents a trade-off between spectral efficiency and overall system performance, and should be selected based on the application requirements.

Table 5.7 further illustrates the effect of varying the master clock rate while keeping N_s and roll-off factor fixed to 2 and 1, respectively. The results show that increasing the master clock rate significantly increases the OBW, since a higher master clock rate enables a higher sampling rate and symbol rate. However, the EVM remains relatively unchanged for master clock rates between 48 MHz and 61.44 MHz, varying only between 11.10% and 11.60%. When maximizing the master clock rate to 61.44 MHz the maximum usable bandwidth is measured to 49.51 MHz.

The lowest EVM is achieved at a master clock rate of 32 MHz, where the occupied

bandwidth is also the smallest. Consequently, lower master clock rates are preferable when minimizing bandwidth usage and maximizing signal quality are prioritized. In contrast, higher master clock rates become beneficial higher data rates are required.

6.4 Signal duration and on-board memory constraints

As shown in Table 5.8, the frame length does not appear to impose any major limitations on the communication system. The specifications of the B205mini-i indicate that the USRP operates as a streaming-based device, continuously transmitting data supplied by the host computer [28]. Consequently, the primary limitation is associated with the host system, as it determines the continuity and rate at which data can be transferred to the USRP hardware.

Although the BER remains zero for all tested frame lengths, the measured EVM gradually increases as the number of transmitted symbols increases. The EVM increases from 6.27% for 1000 symbols to approximately 14.84% for 50000 symbols. This behavior is likely caused by the accumulation of residual phase rotation due to CFO. Even though a shared 10 MHz reference clock was used, small frequency mismatches still remain between the transmitter and receiver. As described in Equation (2.3), CFO introduces a phase rotation that increases linearly with the sample index. Consequently, the accumulated phase error becomes increasingly significant for longer frame durations, causing the received symbols to gradually deviate from their ideal constellation positions.

The results further demonstrate the importance of CFO compensation for longer frame transmissions. When CFO recovery was applied using a 512-bit preamble, the EVM for 10000 symbols was reduced to 8.03%. In comparison, the same transmission without CFO compensation resulted in an EVM of 11.17%, as shown in Table 5.8. This indicates that CFO estimation and compensation become increasingly important as the frame duration increases.

Furthermore, the measured frame duration differs slightly from the computed value. For a transmission consisting of 50000 symbols, the frame duration measured using the oscilloscope was 12.54 ms, corresponding to a deviation of approximately 2.3 ms from the computed duration of 14.836 ms. However, when the theoretical symbol rate of 4 Msym/s, given by Equation (4.2), is used instead, the resulting frame duration for 50000 symbols is 12.5 ms. This estimate agrees much more closely with the measurement, exhibiting a deviation of only 0.04 ms. One possible explanation is that the measured occupied bandwidth underestimates the actual signal bandwidth, consequently leading to an underestimation of the true symbol rate of the system. Despite this discrepancy, the experiments demonstrate that the USRP is capable of handling significantly longer frame durations than those supported by the D-MIMO testbed, which is limited to a maximum signal duration of 76.8 μs, as described in Section 2.4.

6.5 Evaluation of D-MIMO testbed integration

Figure 5.5 shows the effect of using CFO correction on the received constellation. Without the CFO correction, the constellation points are spread in a circular shape instead of forming clusters around ideal symbol positions. This suggests that the received signal is being affected by continuous phase rotation, which is caused by CFO due to the difference between the USRP and the RRH's LO. As a result, the receiver made incorrect symbol decisions, leading to a BER of 0.212 and an EVM of 79.99%. After the CFO correction, the receiver forms four separate clusters. This implies that the CFO correction accounted for the offset, which allowed the receiver to make correct symbol decisions. The EVM and BER also decrease significantly, with a BER value of 0 and an EVM equal to 12.61%.

The CFO correction resulted in a BER equal to 0. However, the EVM could further be improved due to multiple receivers in the testbed. Since the D-MIMO testbed consists of 6 RRHs, the data from the RRHs results in six different received signals. The RRHs are located at different distances from the USRP, and therefore, they are all subject to different channels. This is reflected in Table 5.9, where each RRH exhibits a different EVM value. However, by applying MRC to combine the received signals, a much lower EVM of 4.64% could be obtained. These results clearly demonstrate the effectiveness of D-MIMO systems. Although individual RRHs may experience varying channel conditions and consequently different levels of signal distortion, it can be effectively exploited through combining techniques such as MRC.

6.6 Future work

Future work directions would focus on enabling end-to-end transmission in the D-MIMO testbed, with the USRP acting as the receiving device to achieve full system integration. This would also make it possible to evaluate beamforming using the RRHs and study its impact on system performance. In addition, future work could explore multi-user D-MIMO scenarios using both USRPs as independent transmitting users.

Further extensions could also include higher-order modulation schemes and multi-carrier systems such as orthogonal frequency-division multiplexing. Using higher order modulation techniques can significantly improve the spectral efficiency and throughput of the system, although at the cost of increased susceptibility to channel noise and signal distortion. Similarly, orthogonal frequency-division multiplexing offers enhanced performance in multipath environments.

7

Conclusion

This thesis presented the design, implementation, and evaluation of USRP B205mini-i-based user equipment for use in the Chalmers D-MIMO research testbed. The work was divided into two phases: establishing a point-to-point communication link between the two USRPs and integrating the system into the D-MIMO testbed using CFO estimation and MRC.

In the first phase, a wireless communication link between the USRPs was successfully established. A 15-bit PN-sequence was selected for frame synchronization, and the system achieved zero BER across all tested configurations, with EVM values ranging from 6.27% to 15.31%. In addition, the system supported high symbol rates and wide signal bandwidths, achieving a maximum symbol rate of 27.18 Msym/s, a maximum throughput of 54.25 Mbit/s, and a maximum bandwidth of 49.51 MHz with R_c set to 61.44 MHz.

In the second phase, a CFO estimation based on repeated preambles enabled synchronization without external reference clocks. Using a 512-bit CFO preamble, the system achieved zero BER and an EVM of 8.03%. The system was successfully integrated into the D-MIMO testbed, where MRC combining across all six RRHs achieved an EVM of 4.64%, significantly improving the received signal quality compared to the individual RRHs.

The results demonstrate that low-cost SDR hardware can replace expensive laboratory instruments for user equipment in D-MIMO research, making further testbed experiments more accessible and scalable. However, the testbed is constrained to receive signals with a maximum duration of 76.8 μs, which constrains the maximum frame length and limits the amount of data that can be transmitted during the experiments.

References

[1] W. Jiang and B. Han, *Cellular Communication Networks and Standards*. Springer, 2023.

[2] W. Saad, M. Bennis, and M. Chen, "A vision of 6G wireless systems: Applications, trends, technologies, and open research problems," *IEEE Network*, vol. 34, no. 3, pp. 134–142, May 2020.

[3] E. Björnson and L. Sanguinetti, "Cell-free versus cellular massive mimo: What processing is needed for cell-free to win?" In *IEEE 20th International Workshop on Signal Processing Advances in Wireless Communications (SPAWC)*, Cannes, France, Jul. 2019.

[4] G. Liu et al., "Distributed massive MIMO systems," in *6G Migrates from Communication to XaaS*. Singapore: Springer Nature Singapore, Jan. 2026, pp. 289–323.

[5] V. Grigoriev, A. Komissarov, K. Ryutin, and G. Fokin, "Software-defined radio wireless communication technology design. LibreSDR board validation," in *Systems of Signals Generating and Processing in the Field of on Board Communications*, Moscow, Russian Federation, Mar. 2024.

[6] Ettus Research, *USRP B206mini-i specifications, Revision 379222a-01, initial release*, National Instruments, Aug. 2025. [Online]. Available: `https://www.ettus.com/wp-content/uploads/2025/09/usrp_b206mini-i_specifications.pdf`.

[7] R. Lyons, "Quadrature signals: Complex, but not complicated," 2008. [Online]. Available: `http://www.dspguru.com/info/tutor/quadsig.html`.

[8] F. Jondral, "White gaussian noise – models for engineers," *Frequenz*, vol. 72, Jan. 2017. DOI: `10.1515/freq-2017-0064`.

[9] W. H. T. Rodger E. Ziemer, *Principles of communications: systems, modulation, and noise*, 6th ed. Hoboken, N.J. John Wiley Sons Ltd, 2010.

[10] J. R. Barry and E. A. Lee, *Digital Communications*, 3rd ed. New York: McGraw, 2004.

[11] V. K. Garg and Y.-C. Wang, "3 - transmission of digital signals," in *The Electrical Engineering Handbook*, W.-K. CHEN, Ed., Burlington: Academic Press, 2005, pp. 965–970, ISBN: 978-0-12-170960-0. DOI: https://doi.org/10.1016/B978-012170960-0/50071-2. [Online]. Available: https://www.sciencedirect.com/science/article/pii/B9780121709600500712.

[12] M. Zafari, D. Pandey, and R. Doost-Mohammady, *An analytical and experimental study of distributed uplink beamforming in the presence of carrier frequency offsets*, Aug. 2025. DOI: 10.48550/arXiv.2508.08506.

[13] E. Agrell, J. Lassing, E. G. Strom, and T. Ottosson, "Gray coding for multilevel constellations in gaussian noise," *IEEE Transactions on Information Theory*, vol. 53, no. 1, pp. 224–235, 2007. DOI: 10.1109/TIT.2006.887070.

[14] E. Cubukcu, "Root raised cosine (RRC) filters and pulse shaping in communication systems," NASA, Tech. Rep., May 2012, Avionic Systems Analysis. Accessed: Apr. 22, 2026. [Online]. Available: https://ntrs.nasa.gov/api/citations/20120008631/downloads/20120008631.pdf.

[15] N. Alagha and P. Kabal, "Generalized raised-cosine filters," *IEEE Transactions on Communications*, vol. 47, no. 7, pp. 989–997, 1999. DOI: 10.1109/26.774849.

[16] R. A. Shafik, M. S. Rahman, and A. R. Islam, "On the extended relationships among EVM, BER and SNR as performance metrics," in *Proc. IEEE International Conference on Electrical and Computer Engineering (ICECE)*, Dhaka, Bangladesh, Dec. 2006, pp. 408–411.

[17] A. Grami, "Chapter 6 - baseband digital transmission," in *Introduction to Digital Communications*, Boston: Academic Press, 2016, pp. 265–297, ISBN: 978-0-12-407682-2. DOI: https://doi.org/10.1016/B978-0-12-407682-2.00006-5. [Online]. Available: https://www.sciencedirect.com/science/article/pii/B9780124076822000065.

[18] J. G. Proakis and M. Salehi, *Digital Communications*, 5th ed. New York: McGraw-Hill, 2008.

[19] R. Mutagi, "Pseudo noise sequences tor engineers," *Electronics & communication engineering journal*, vol. 1, 2N–3, 1996.

[20] D. V. Sarwate and M. B. Pursley, "Crosscorrelation properties of pseudorandom and related sequences," *Proceedings of the IEEE*, vol. 68, no. 5, pp. 593–619, May 1980.

[21] J. Massey, "Optimum frame synchronization," *IEEE Transactions on Communications*, vol. 20, no. 2, pp. 115–119, 1972. DOI: 10.1109/TCOM.1972.1091127.

[22] G. J. González, F. H. Gregorio, J. Cousseau, S. Werner, and R. Wichman, "Data-aided cfo estimators based on the averaged cyclic autocorrelation," *Signal Processing*, vol. 93, no. 1, pp. 217–229, 2013, ISSN: 0165-1684. DOI: https://doi.org/10.1016/j.sigpro.2012.07.032. [Online]. Available: https://www.sciencedirect.com/science/article/pii/S0165168412002629.

[23] S. Roy and P. Fortier, "Maximal-ratio combining architectures and performance with channel estimation based on a training sequence," *IEEE Transactions on Wireless Communications*, vol. 3, no. 4, pp. 1154–1164, 2004. DOI: 10.1109/TWC.2004.828022.

[24] Q. Chaudhari. "Maximum ratio combining (mrc)." Accessed: 2026-05-13. [Online]. Available: https://wirelesspi.com/maximum-ratio-combining-mrc/.

[25] A. Rao, E. Bogatin, and M. Piket-May, "Metrics for acceptable oscilloscope bandwidth," *IEEE Transactions on Instrumentation and Measurement*, vol. 74, Mar. 2025.

[26] M. E. Haque, M. G. Rashed, and M. H. Kabir, "A comprehensive study and performance comparison of m-ary modulation schemes for an efficient wireless mobile communication system," *arXiv preprint arXiv:1203.1778*, 2012.

[27] Y. Han, Q. Li, Y. Wang, K. Gong, P. Liu, and Y. Sun, "Study on crystal oscillator frequency drift model and performance of low orbit satellite," in *2022 IEEE 10th Joint International Information Technology and Artificial Intelligence Conference (ITAIC)*, vol. 10, 2022, pp. 1622–1626. DOI: 10.1109/ITAIC54216.2022.9836839.

[28] Ettus Research, "Usrp b200mini series data sheet," National Instruments, Tech. Rep., 2019, Accessed: 2026-05-13. [Online]. Available: https://www.ettus.com/wp-content/uploads/2019/01/USRP_B200mini_Data_Sheet.pdf.

[29] A. M. Wyglinski, D. P. Orofino, M. N. Ettus, and T. W. Rondeau, "Revolutionizing software defined radio: Case studies in hardware, software, and education," *IEEE Communications Magazine*, vol. 54, no. 1, pp. 68–75, 2016. DOI: 10.1109/MCOM.2016.7378428.

Appendices

A

Simulation Results for CFO Estimation Performance

Simulation results for CFO recovery are presented in Table A.1. The simulations were performed with an SNR of 15 dB, a fractional CFO of $\Delta f / f_s = 5.0 \times 10^{-6}$, and a phase offset $\phi = \frac{\pi}{12}$. For each preamble length, 100 simulations were performed.

Table A.1: Simulated tradeoff between preamble symbol overhead and CFO estimation performance

Preamble length [bits]	BER	EVM	Fractional Deviation	Maximum fractional deviation
32	0.38	112.89%	320%	900%
64	0.19	71.63%	100%	420%
128	0.03	32.34%	40%	140%
256	0	13.48%	20%	40%
512	0	10.12%	0%	20%

The fractional deviation, expressed as a percentage, is calculated as

$$\text{Fractional deviation} = \frac{|\frac{\Delta f}{f_s} - \hat{\epsilon}|}{\frac{\Delta f}{f_s}} \times 100 \tag{A.1}$$

where $\hat{\epsilon}$ denotes the estimated CFO.

B

USRP B205mini-i Hardware Overview

The USRP is an SDR developed by Ettus Research and National Instruments [29]. The model used in this project is the USRP B205mini-i, which operates over a frequency range of 70 MHz to 6 GHz and supports a maximum instantaneous bandwidth of 56 MHz.

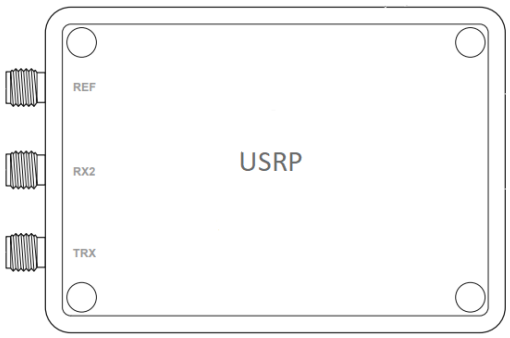

Figure B.1: USRP layout. [6]

As shown in Figure B.1, the B205mini-i includes multiple RF ports for both transmission and reception. One port is used for RF transmission, another for RF reception, and an additional REF port provides a reference clock signal used for hardware synchronization between devices. The USRP is controlled through a MATLAB interface using the UHD drivers, which enable real-time transmission and reception of IQ samples [6].

The B205mini-i also includes a reference port. This port allows the device to be synchronized with an external 10 MHz reference signal (typically provided by a function generator) to improve carrier frequency accuracy. In addition, the same port can be used to receive a pulse-per-second signal for timing synchronization, enabling multiple devices to operate with aligned time bases.

DEPARTMENT OF ELECTRICAL ENGINEERING
CHALMERS UNIVERSITY OF TECHNOLOGY
Gothenburg, Sweden
www.chalmers.se

CHALMERS
UNIVERSITY OF TECHNOLOGY